Ultrasoft slip-mediated bending in few-layer graphene

Edmund Han [1,5], Jaehyung Yu [2,5], Emil Annevelink[2], Jangyup Son[2], Dongyun A. Kang[2], Kenji Watanabe [3], Takashi Taniguchi[3], Elif Ertekin[2,4], Pinshane Y. Huang [1,4]* and Arend M. van der Zande [2,4]*

Continuum scaling laws often break down when materials approach atomic length scales, reflecting changes in their underlying physics and the opportunities to access unconventional properties. These continuum limits are evident in two-dimensional materials, where there is no consensus on their bending stiffnesses or how they scale with thickness. Through combined computational and electron microscopy experiments, we measure the bending stiffness of graphene, obtaining 1.2–1.7 eV for a monolayer. Moreover, we find that the bending stiffness of few-layer graphene decreases sharply as a function of bending angle, tuning by almost 400% for trilayer graphene. This softening results from shear, slip and the onset of superlubricity between the atomic layers and corresponds with a gradual change in scaling power from cubic to linear. Our results provide a unified model for bending in two-dimensional materials and show that their multilayers can be orders of magnitude softer than previously thought, among the most flexible electronic materials currently known.

Two-dimensional (2D) materials exhibit a host of unusual properties that arise from their anisotropic atomic structure and bonding. For example, the 3D Young's modulus of few-layer graphene (FLG) is 1 TPa (ref. [1]), three orders of magnitude larger than its 4.6 GPa shear modulus[2]. Bending, a process that couples in-plane and out-of-plane motion, provides an opportunity to test the effects of anisotropy on the mechanical properties of 2D materials. In particular, interlayer slip has been shown to be a dominant mechanism for relieving stress at van der Waals interfaces[3,4] and in multiwalled carbon nanotubes[5] and nanotube bundles[6]. Slip should have similarly important impacts on the bending properties of 2D materials. Bending stiffness takes on practical significance in a new generation of devices where 2D materials are highly curved and shaped into complex 3D architectures[7–11]. Highly curved 2D materials have promise across soft robotics and deformable electronics because they combine the high charge carrier mobilities of hard materials with the pliability of soft materials. In these systems, the bending stiffness governs the 3D nanoscale deformations of 2D materials, the structure and onset of folding[12], rippling[13], buckling[13] and crumpling[7], as well as the interfacial mechanics[14,15] of deformed structures on surfaces.

Yet, after more than a decade, there is still no single model that describes the widely divergent measurements of bending stiffness in monolayer graphene and FLG[2,12,16–18]. Unlike graphene's well-known in-plane properties such as its Young's modulus and breaking stress[1,19,20], the small bending stiffness of FLG has proven difficult to characterize. FLG exhibits markedly different mechanical properties from bulk graphite[1,21–24] because structural imperfections in bulk systems overshadow the intrinsic properties of the individual atomic layers. In the few-layer limit, techniques such as nanoindentation, electrostatic actuation, atomistic simulations and measurements of nanoscale fold morphologies[12,17,18,25–29] have produced a broad range

of bending stiffness for FLG, which appear to be in conflict. For monolayer graphene, literature values for its bending stiffness range from 0.83 to 10,000 eV (refs. [9,16,27,28,30–32]). Furthermore, the reported bending stiffness of bilayer graphene ranges across two orders of magnitude, from 3.4 to 160 eV, while values for trilayer graphene range from 7 to 690 eV (refs. [12,17,18,27,31]). There is also little agreement on the mechanisms and scaling laws that govern the bending of FLG: linear, quadratic and cubic scaling of bending stiffness with thickness have all been reported[2,12,16–18]. Some inconsistencies arise from the difficulty of measuring the intrinsic bending stiffness of FLG without the contributions from extrinsic stiffening from out-of-plane corrugations or in-plane strain. Another possibility is that these discrepancies reflect real differences in bending stiffness in different physical regimes. When highly bent, 2D materials may be governed by fundamentally different mechanics than in nearly flat geometries, and they may undergo dynamic transitions in bending properties as they are bent and flattened during operation. Yet, the mechanical behaviour of 2D materials spanning from low to high bending regimes is not well understood.

In this work, we aim to produce a unified understanding of bending in few-layer 2D materials across curvature regimes. To tackle this challenge, we fabricated heterostructures of FLG draped over atomically sharp steps of hexagonal boron nitride (hBN), as illustrated in Fig. 1a. These structures allow us to systematically vary the thickness and degree of curvature of the graphene, then analyse their bending through cross-sectional imaging with aberration-corrected scanning transmission electron microscopy (STEM). As shown in Fig. 1b, the graphene is placed perpendicularly across hBN steps using established dry aligned transfer techniques (see Methods). We confirmed the cleanliness and uniformity of the heterostructure with atomic force microscopy (AFM) and Raman spectroscopy (Supplementary Methods 1.1 and Supplementary Figs. 1 and 2),

[1]Department of Materials Science and Engineering, University of Illinois at Urbana-Champaign, Urbana, IL, USA. [2]Department of Mechanical Science and Engineering, University of Illinois at Urbana-Champaign, Urbana, IL, USA. [3]National Institute for Materials Science, Tsukuba, Japan. [4]Materials Research Laboratory, University of Illinois at Urbana-Champaign, Urbana, IL, USA. [5]These authors contributed equally: Edmund Han, Jaehyung Yu. *e-mail: pyhuang@illinois.edu; arendv@illinois.edu
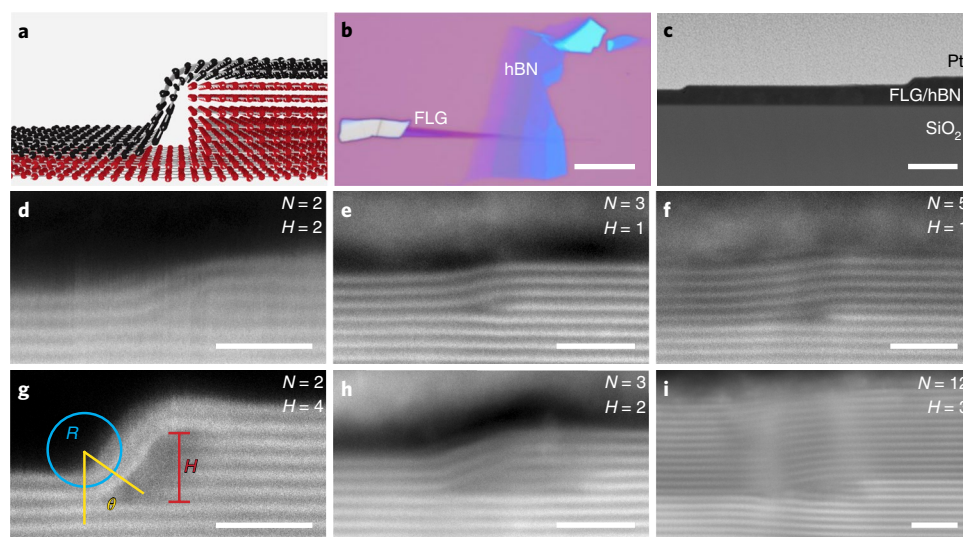
Fig. 1 | Fabrication and STEM imaging of curved FLG on hBN steps. a, Schematic of the heterostructure. A graphene bilayer (black) is shown on top of a hBN step (red). **b**, Optical image of FLG transferred over an exfoliated hBN flake. Colour gradient of hBN indicates varying thickness and presence of steps in the flake. Scale bar, 10 μm. **c**, Low-magnification ADF-STEM image of the stair-step structure in cross-section. From bottom to top, the layers in cross-section are Si/SiO₂/hBN/FLG/amorphous carbon/Pt (not all layers are distinguishable). Most prominent are two large hBN steps. Scale bar, 100 nm. **d–i**, ADF-STEM images of N-layer graphene over H-layer-thick hBN steps. We observe varying graphene bending profiles for different N and H. We parameterize the bending profile according to the radius of curvature R, bending angle θ and step height H, as indicated in **g**. Throughout the text, we define the bending angle as the angle subtending the two lines perpendicular to the straight sections on either side of the bend. Scale bars, 2 nm (**d–i**).

then prepared cross-sectional TEM samples using standard focused ion beam lift-out procedures (see Methods). An example of a resulting sample is shown in the low-magnification STEM image in Fig. 1c; each sample contains multiple hBN steps with varying heights. Figure 1d–i shows annular dark-field (ADF) STEM images of FLG on hBN steps with varying FLG thickness and hBN step height. Electron microscopy provides a powerful platform for measuring the mechanical properties of nanomaterials by enabling studies of their conformation and strain at atomic resolution[28,33–36]. We imaged 22 individual steps with FLG thicknesses of 1–12 layers and hBN step heights of 1–19 layers (for the raw images of each step see Supplementary Figs. 3–5). In these images, the bending profile of FLG and the corresponding mechanics are described by two critical parameters, the radius of curvature R and bending angle θ, as illustrated in Fig. 1g. Throughout the text, we define the bending angle as the angle subtending the two lines perpendicular to the straight sections on either side of the bend. We observe a wide range of bending angles (8.5–63°) and radii of curvature as small as 1.0 nm, comparable to the inner radii of carbon nanotubes.

Here, we study how the conformation of FLG (described by R and θ) varies with the controlled parameters: FLG thickness (N) and hBN step height (H). Figure 2a shows the bending angle as a function of hBN step height for two different FLG thicknesses, while Fig. 2b shows the radius of curvature versus the number of graphene layers, colour-coded by hBN step height. These plots demonstrate clear relationships between the geometric parameters: higher bending angles are associated with taller steps and thicker FLG samples have larger radii of curvature. To relate the bending profile of FLG to its mechanics, we apply a simple model in which the conformation is governed by competition between the graphene/hBN interfacial adhesion energy and the FLG bending energy. Solving for the minimum energy, we obtain an equation that relates the bending stiffness of FLG to its equilibrium conformation (see Supplementary Methods 1.2 and Supplementary Fig. 6). This model is similar to the elastic shell model used to describe carbon nanotube mechanics[37,38]. We use this equation to

calculate the bending stiffness from geometric parameters measured in the STEM images:

$$B = R\Gamma\left(\frac{H - 2R(1 - \cos\theta)}{\sin^2\theta}\right) \tag{1}$$

where B is the bending stiffness, $\Gamma = 0.126\,\mathrm{J\,m^{-2}}$ is the graphene/hBN interfacial adhesion energy[39], H is the hBN step height, R is the radius of curvature and θ is the bending angle. This equation assumes that the in-plane strain energy is negligible because incommensurate hBN/graphene interfaces are superlubric[3], which, in the absence of interfacial contamination, prevents the build-up of in-plane stress in the laminated top-layer graphene[40]. See Supplementary Methods 1.3 for an additional discussion of error sources.

We first use these methods to extract the bending stiffness of monolayer graphene. Analysing the two steps shown in Supplementary Fig. 3a,b we obtain bending stiffnesses of $B_{\mathrm{ml}} = 1.2 \pm 0.11\,\mathrm{eV}$ and $B_{\mathrm{ml}} = 1.7 \pm 0.50\,\mathrm{eV}$, respectively (the stated error represents the 95% confidence bounds). We also performed density functional theory (DFT) analysis of monolayer graphene and found a deformation-independent bending stiffness of 1.4 eV (Supplementary Fig. 7). Although the bending stiffness of monolayer graphene has long been a topic of debate[9,16,27,28,30], both our experimental and theoretical values are consistent with previous DFT results from the literature[30] and the experimental value of 1.2 eV derived from graphite phonon modes[41]. These values are comparable to other experimental values for the intrinsic bending stiffness, but significantly lower than the effective bending stiffness of 10^2 to $10^4\,\mathrm{eV}$ measured in micrometre-scale suspended graphene[9], where factors such as buckles and thermal rippling dominate the bending properties.

Next we analyse the bending stiffness of FLG. Figure 2c plots the extracted bending stiffness as a function of thickness (black). Our measurements yield low values for B, near or below the lowest FLG bending stiffnesses reported in the literature. For example, we report bending stiffness values between 2.6 and 5.8 eV for
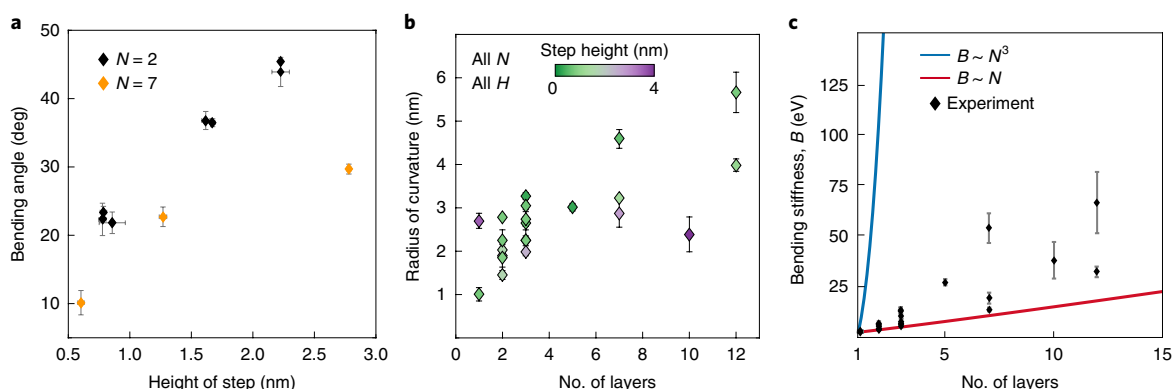
Fig. 2 | Measurement of bending stiffness from STEM images. a, Plot of bending angle versus step height H for two- and seven-layer graphene. For a given number of graphene layers N, the bending angle increases with hBN step height. **b**, Plot of radius of curvature versus thickness for all step heights and graphene thicknesses. Each point is colour-coded by hBN step height. The radius of curvature generally increases with thickness. **c**, Experimental measurements of bending stiffness versus thickness for FLG. Experimental values (black) are extracted using geometric parameters from the STEM images. Bending models representing cubic (blue) and linear (red) scaling are shown for comparison. Error bars for geometric parameters and bending stiffness values represent 95% confidence bounds as determined by four independent geometric measurements and their error propagation.

bilayer graphene, while previously reported values range from 3.4 to 160 eV (refs. [12,17,18,27,31]). We compare these values to upper and lower bounds of FLG bending stiffness from continuum mechanics plate theory, where 2D materials may be described as a single or series of stacked plates, depending on the interlayer coupling strength. The bending stiffness of a single plate scales with the cube of its thickness, or $B \propto Y_{3D} t^3$ where t is the thickness and Y_{3D} is the 3D Young's modulus. The blue line in Fig. 2c represents the single-plate continuum model, modified for the discrete nature of FLG[17,18]: $B = \frac{Y_{3D} \times t_0^3}{12}(N^3 - N) + B_{ml}N$, where $t_0 = 0.334$ nm is the interlayer separation[13], $B_{ml} = 1.4$ eV is the intrinsic monolayer graphene bending stiffness[30] and N is the number of layers. In contrast, for a stack of frictionless plates, the bending stiffness scales linearly with layer number, $B = B_{ml}N$ (red line, Fig. 2c); this lowered scaling power reflects the ability of the layers to move independently. Our experimental data are close to the lower limit given by the linear model, indicating weak interlayer interactions in the regimes measured. Intriguingly, we also observe a spread of B for each FLG thickness. As we show below, these variations indicate an angle dependence of the bending stiffness and its scaling laws.

In Fig. 3, we model the bending of FLG using DFT[42,43]. Figure 3a plots the bending stiffness of one- to five-layer graphene as a function of bending angle. In these simulations, graphene is bent along the zigzag $\langle \bar{2}110 \rangle$ direction (see Supplementary Methods 1.4 and Supplementary Figs. 7–9 for simulation details and results for the armchair $\langle \bar{1}100 \rangle$ direction). In Fig. 3a, the bending stiffness for each FLG thickness $N > 1$ decreases sharply with increasing angle and gradually levels off above a threshold angle around 40°. The variations in Fig. 3a are significant; for example, the bending stiffness of five-layer graphene decreases from 51 eV at 4° to 8.5 eV at 80°. Figure 3b directly compares experimental (filled symbols) and DFT measurements (empty symbols) of bending stiffness for one- to four-layer graphene, colour-coded by bending angle. Supplementary Fig. 10 also plots the experimental bending stiffness versus bending angle and curvature. We obtain remarkable agreement between theory and experiment; both show a clear decrease in bending stiffness with increasing bending angle. An important implication of these results is that the bending stiffness of FLG is not a single value for a given thickness, but instead depends on the geometry in which it is measured, a result that may partially explain the wide range of reported bending stiffness in the literature.

We also find that the bending stiffness follows different scaling laws depending on the bending angle. We applied power-law

fits $B = cN^\gamma$ to the DFT simulations (Supplementary Fig. 11) as well as simulations using classical potentials, which allowed us to access larger systems up to $N = 10$ and lower angles down to 1° (see Methods and Supplementary Fig. 12). At the limits of low and high angles, we observe scaling laws that approach the predictions from continuum mechanics. For a low angle of $\theta = 4.4°$, we obtain $\gamma = 2.2 \pm 0.23$ (blue line, Fig. 3b) from the DFT fits; using classical potentials, we find the scaling law continues to increase towards cubic at the lowest angles we simulated, yielding $\gamma = 3.1 \pm 0.67$ for $\theta = 1°$. Conversely, for high bending angles, we obtain a nearly linear scaling through both simulation methods; for example, we obtain $\gamma = 1.1 \pm 0.022$ from the DFT at $\theta = 81°$ (red line, Fig. 3b). Between these limits, the scaling power gradually decreases as the bending angle increases (Supplementary Fig. 11). Strikingly, our results show that above a threshold angle around 40°, FLG exhibits a nearly linear scaling law characteristic of a stack of frictionless plates, where each layer has the 1.5 eV bending stiffness of monolayer graphene. These results indicate the onset of superlubricity between the atomic layers of graphene at high bending angles. Figure 4a,b presents schematics of the two primary atomic deformations that can accommodate the differential stress induced by bending in 2D materials: in-plane strain within the layers (Fig. 4a) or shear and slip between layers (Fig. 4b). These models can be readily distinguished by comparing the number of atoms in each layer along the bend, which remains constant in the in-plane strain case but increases radially in the slip case. In Fig. 4c, we compare these models to a bright-field STEM image of curved 12-layer graphene. The number of atomic columns in each layer in the STEM image increases radially, confirming that the bending mechanism in FLG is dominated by interlayer shear and slip.

Next, we model the impact of interlayer slip on the atomic structure of FLG. The inset of Fig. 4d shows a profile for curved bilayer graphene where the curvature is accommodated entirely by slip. This cartoon is drawn flat (that is, in cylindrical coordinates) to highlight the interlayer registry. Here, bending produces an effective lattice mismatch between adjacent layers that increases with bending angle. This behaviour is equivalent to the formation of extended dislocations or solitons[4] between layers. Adapting the concept of geometrically necessary dislocations[44], the number of dislocations per layer is given by $N = t_0\theta/|\mathbf{b}|$, where t_0 is the interplanar spacing and $\mathbf{b}$ is the Burgers vector as defined in Supplementary Fig. 9. This equation predicts the angle at which the outer layer contains exactly one more atomic column than the layer below, or equivalently the angle at which a full dislocation is present between adjacent layers.
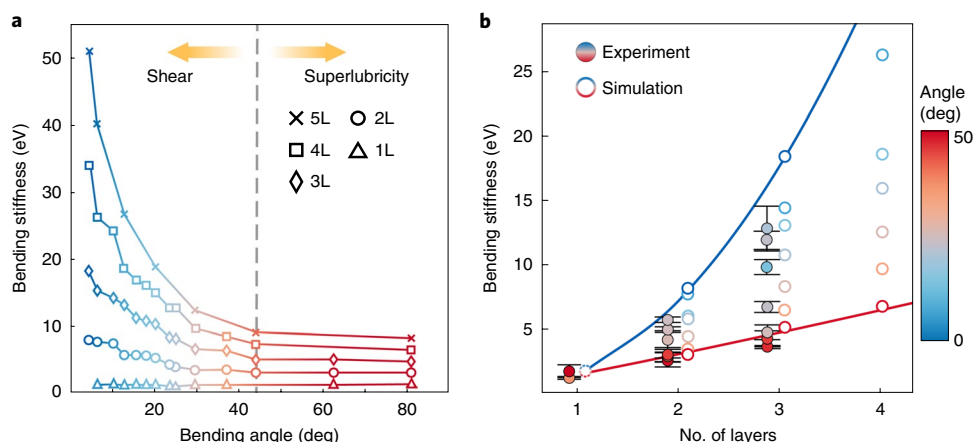
Fig. 3 | DFT calculations of bending stiffness in FLG and comparison with experiment. a, Plot of DFT-calculated bending stiffness versus bending angle for monolayer (1L) to five-layer (5L) graphene, bent along the zigzag direction. The bending stiffness decreases with bending angle for all $N > 1$ and plateaus at ~41°. **b**, Comparison of DFT and experimental bending stiffnesses versus thickness for monolayer to four-layer graphene. Open and filled symbols represent bending stiffness from DFT and experiment, respectively. Data are colour-coded by the bending angle θ. Error bars for experimental bending stiffness values represent 95% confidence bounds, as determined by error propagation of geometric measurements. The DFT and experimental values exhibit a strong quantitative match, and both indicate a strong angle dependence for the bending stiffness. Power-law fits to the DFT simulation, $B \propto N^\gamma$, yield $\theta = 4.4°$ for $\gamma = 1.1 \pm 0.022$ (blue line) and $\theta = 81°$ for $\theta = 81°$ (red line). These fits show that the thickness scaling of bending stiffness changes with the curvature angle.
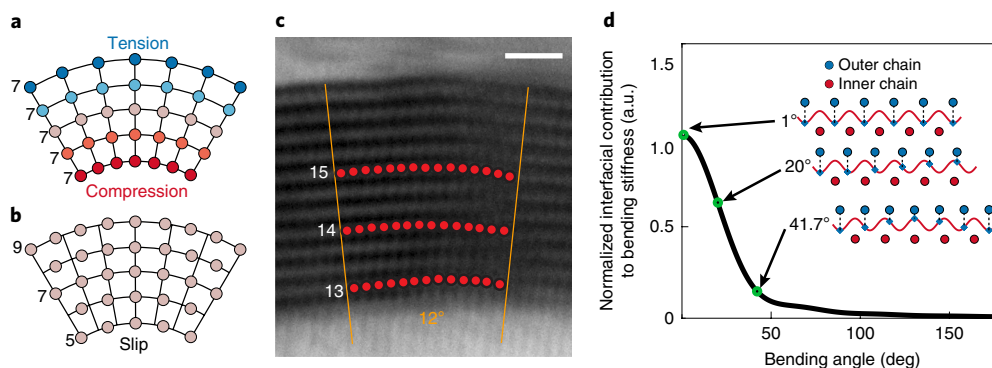

Fig. 4 | Atomic-scale bending mechanisms in FLG. a, Schematic for bending that is accommodated by in-plane strain in the graphene layers. **b**, Schematic for bending that is accommodated through interlayer shear and slip. **c**, Bright-field STEM image of 12-layer graphene bent to 40°. The number of atomic columns in the arc is higher for the outer graphene layers than for the inner layers, indicating bending consistent with the shear-slip model. Scale bar, 1 nm. **d**, Plot of the interfacial contribution to bending stiffness versus bending angle, derived from a simplified, two-chain Frenkel–Kontorova model. The interfacial contribution to bending stiffness decreases with bending angle and plateaus at around 40°, similarly to the DFT results in Fig. 3a. Inset: Cartoons of the interlayer registry of atoms in a 1D model for curved bilayer graphene, where the curvature is accommodated entirely by slip between layers. The atomic positions are plotted in cylindrical coordinates to show how atoms are aligned radially along the curve. The registry between layers decreases as the bending angle increases.

This value is dependent on the crystallographic orientation of the bend: 41.7° for bending along the zigzag direction and 24–36° for bending in the armchair direction. These angles correspond directly with the angular thresholds observed in the DFT simulations in Fig. 3a and Supplementary Fig. 9, demonstrating that a simple dislocation model can be used to predict the bending angles above which superlubricity dominates.

In the shear-slip bending mechanism, the bending stiffness of 2D materials can be separated into two components: (1) the intrinsic bending stiffness of individual graphene layers and (2) the contribution from interfacial interactions between layers. Figure 4d plots the interfacial contribution to bending stiffness as a function of bending angle, given by a simplified Frenkel–Kontorova (F–K) model (for details see Supplementary Methods 1.5). The F–K model is commonly used to describe interfacial interactions in thin films,

including the dynamics of friction[45] and the formation of solitons in bilayer graphene[4]. In Fig. 4d, we apply a simplified F–K model to describe curved bilayer graphene: each layer comprises a linear 1D chain of atoms connected by springs, and the atoms experience a sinusoidal atomic potential from the adjacent layer. By assuming an infinite in-plane spring constant—or equivalently, no in-plane strain—we force the system to follow the shear-slip bending mechanism to isolate and directly probe its effect on the bending stiffness. Here, the bending energy represents the change in interfacial energy resulting from changes in atomic registry between the layers. Notably, Fig. 4d qualitatively reproduces the drop-off in bending stiffness and the threshold angles seen in our experiment and DFT simulations. These results directly show that our experimental observation of FLG's angle-dependent bending stiffness can be explained entirely by shear and slip.

Put together, the analyses above unite continuum and atomic-scale models to predict, calculate and experimentally verify the phenomenon of slip-induced softening of FLG. Our results show that FLG relieves bending stress primarily through shear and slip between layers rather than in-plane strain. As FLG is gradually bent, its interlayer interactions transition between two limits: the strong coupling characteristic of Bernal-stacked graphite[4] and the weak, superlubric interactions of multiwalled carbon nanotubes[5]. This change in atomic registry and interlayer coupling directly results in a dramatic reduction of bending stiffness to $B \propto N^\gamma$, or equivalently $B \propto t^\gamma$, where $1 < \gamma < 3$, rather than the $B \propto t^3$ behaviour of conventional thin films. Finally, we show that a simple dislocation model can predict the angular threshold for bending-induced superlubricity when a full dislocation is present between each layer. These behaviours occur in 2D materials because of their high anisotropy and low energy barrier for slip between atomic layers. For Bernal-stacked graphene, this energetic barrier is less than 2.1 meV per atom[4], an order of magnitude lower than the 70–90 meV per atom barrier for slip in face-centred cubic nickel[46].

These results have significant implications for the mechanical properties of 2D materials and devices. Our findings indicate a new lower limit for the fabrication of ultrasoft, high-mobility electronic nanodevices. For ten-layer graphene, we show that the bending stiffness can be as low as 18 eV, three orders of magnitude lower than the bending stiffness predicted by conventional thin-film mechanics[18]. Although we have focused on the properties of graphene, our conclusions should generalize to other van der Waals-bonded materials. Finally, these results will be important for the design of new classes of highly curved nanosystems such as nanoelectromechanical systems, stretchable electronics and origami structures made from 2D materials.

Online content

Any methods, additional references, Nature Research reporting summaries, source data, extended data, supplementary information, acknowledgements, peer review information; details of author contributions and competing interests; and statements of data and code availability are available at https://doi.org/10.1038/s41563-019-0529-7.

References

1. Lee, C., Wei, X., Kysar, J. W. & Hone, J. Measurement of the elastic properties and intrinsic strength of monolayer graphene. *Science* **321**, 385–388 (2008).
2. Shen, Y. & Wu, H. Interlayer shear effect on multilayer graphene subjected to bending. *Appl. Phys. Lett.* **100**, 101904–101909 (2012).
3. Song, Y. et al. Robust microscale superlubricity in graphite/hexagonal boron nitride layered heterojunctions. *Nat. Mater.* **17**, 894–899 (2018).
4. Alden, J. S. et al. Strain solitons and topological defects in bilayer graphene. *Proc. Natl Acad. Sci. USA* **110**, 11256–11260 (2013).
5. Cumings, J. & Zettl, A. Low-friction nanoscale linear bearing realized from multiwall carbon nanotubes. *Science* **289**, 602–604 (2000).
6. Yakobson, B. I., Samsonidze, G. & Samsonidze, G. G. Atomistic theory of mechanical relaxation in fullerene nanotubes. *Carbon* **38**, 1675–1680 (2000).
7. Zang, J. et al. Multifunctionality and control of the crumpling and unfolding of large-area graphene. *Nat. Mater.* **12**, 321–325 (2013).
8. Kang, P., Wang, M. C., Knapp, P. M. & Nam, S. Crumpled graphene photodetector with enhanced, strain-tunable, and wavelength-selective photoresponsivity. *Adv. Mater.* **28**, 4639–4645 (2016).
9. Blees, M. K. et al. Graphene kirigami. *Nature* **524**, 204–207 (2015).
10. Lee, W. et al. Two-dimensional materials in functional three-dimensional architectures with applications in photodetection and imaging. *Nat. Commun.* **9**, 1417 (2018).
11. Miskin, M. Z. et al. Graphene-based bimorphs for micron-sized, autonomous origami machines. *Proc. Natl Acad. Sci. USA* **115**, 466–470 (2018).
12. Chen, X., Yi, C. & Ke, C. Bending stiffness and interlayer shear modulus of few-layer graphene. *Appl. Phys. Lett.* **106**, 101907 (2015).
13. Bao, W. et al. Controlled ripple texturing of suspended graphene and ultrathin graphite membranes. *Nat. Nanotechnol.* **4**, 562–566 (2009).
14. Brennan, C. J., Nguyen, J., Yu, E. T. & Lu, N. Interface adhesion between 2D materials and elastomers measured by buckle delaminations. *Adv. Mater. Interfaces* **2**, 1500176 (2015).
15. Jiang, T., Huang, R. & Zhu, Y. Interfacial sliding and buckling of monolayer graphene on a stretchable substrate. *Adv. Funct. Mater.* **24**, 396–402 (2013).
16. Akinwande, D. et al. A review on mechanics and mechanical properties of 2D materials—graphene and beyond. *Extreme Mech. Lett.* **13**, 42–77 (2017).
17. Zhang, D. B., Akatyeva, E. & Dumitrică, T. Bending ultrathin graphene at the margins of continuum mechanics. *Phys. Rev. Lett.* **106**, 3–6 (2011).
18. Koskinen, P. & Kit, O. O. Approximate modeling of spherical membranes. *Phys. Rev. B* **82**, 1–5 (2010).
19. Bunch, J. S. et al. Impermeable atomic membranes from graphene sheets. *Nano Lett.* **8**, 2458–2462 (2008).
20. Lopez-Polin, G. et al. Increasing the elastic modulus of graphene by controlled defect creation. *Nat. Phys.* **11**, 26–31 (2014).
21. Tapasztó, L. et al. Breakdown of continuum mechanics for nanometre-wavelength rippling of graphene. *Nat. Phys.* **8**, 739–742 (2012).
22. Nikiforov, I., Tang, D. M., Wei, X., Dumitrică, T. & Golberg, D. Nanoscale bending of multilayered boron nitride and graphene ribbons: experiment and objective molecular dynamics calculations. *Phys. Rev. Lett.* **109**, 1–5 (2012).
23. Yang, Z. et al. Mechanical properties of atomically thin boron nitride and the role of interlayer interactions. *Nat. Commun.* **8**, 15815 (2017).
24. Rooney, A. P. et al. Anomalous twin boundaries in two dimensional materials. *Nat. Commun.* **9**, 3597 (2018).
25. Poot, M. & van der Zant, H. S. J. Nanomechanical properties of few-layer graphene membranes. *Appl. Phys. Lett.* **92**, 063111 (2008).
26. Booth, T. J. et al. Macroscopic graphene membranes and their extraordinary stiffness. *Nano Lett.* **8**, 2442–2446 (2008).
27. Lindahl, N. et al. Determination of the bending rigidity of graphene via electrostatic actuation of buckled membranes. *Nano Lett.* **12**, 3526–3531 (2012).
28. Zhao, J. et al. Two-dimensional membrane as elastic shell with proof on the folds revealed by three-dimensional atomic mapping. *Nat. Commun.* **6**, 8935 (2015).
29. Kvashnin, D. G. & Sorokin, P. B. Effect of ultrahigh stiffness of defective graphene from atomistic point of view. *J. Phys. Chem. Lett.* **6**, 2384–2387 (2015).
30. Ertekin, E., Chrzan, D. C. & Daw, M. S. Topological description of the Stone–Wales defect formation energy in carbon nanotubes and graphene. *Phys. Rev. B* **79**, 155421 (2009).
31. Guo, Y., Qiu, J. & Guo, W. Mechanical and electronic coupling in few-layer graphene and hBN wrinkles: a first-principles study. *Nanotechnology* **27**, 505702 (2016).
32. Wei, Y., Wang, B., Wu, J., Yang, R. & Dunn, M. L. Bending rigidity and Gaussian bending stiffness of single-layered graphene. *Nano Lett.* **13**, 26–30 (2013).
33. Iijima, S., Brabec, C., Maiti, A. & Bernholc, J. Structural flexibility of carbon nanotubes. *J. Chem. Phys.* **104**, 2089–2092 (1996).
34. Warner, J. H. et al. Dislocation-driven deformations in graphene. *Science* **337**, 209–212 (2012).
35. Kim, K. et al. Ripping graphene: preferred directions. *Nano Lett.* **12**, 293–297 (2012).
36. Casillas, G., Liao, Y., Jose-Yacaman, M. & Marks, L. D. Monolayer transfer layers during sliding at the atomic scale. *Tribol. Lett.* **59**, 45 (2015).
37. Yakobson, B. I., Brabec, C. J. & Bernolc, J. Nanomechanics of carbon tubes: instabilities beyond linear response. *Phys. Rev. Lett.* **76**, 2511–2514 (1996).
38. Ru, C. Q. Effective bending stiffness of carbon nanotubes. *Phys. Rev. B* **62**, 9973–9976 (2000).
39. Sanchez, D. A. et al. Mechanics of spontaneously formed nanoblisters trapped by transferred 2D crystals. *Proc. Natl Acad. Sci. USA* **115**, 7884–7889 (2018).
40. Woods, C. R. et al. Commensurate–incommensurate transition in graphene on hexagonal boron nitride. *Nat. Phys.* **10**, 451–456 (2014).
41. Nicklow, R., Wakabayashi, N. & Smith, H. G. Lattice dynamics of pyrolytic graphite. *Phys. Rev. B* **5**, 4951–4962 (1972).
42. Hohenberg, P. & Kohn, W. Inhomogeneous electron gas. *Phys. Rev. B* **136**, 864–871 (1964).
43. Kohn, W. & Sham, L. J. Self-consistent equations including exchange and correlation effects. *Phys. Rev. A* **140**, 1133–1138 (1965).
44. Nye, J. F. Some geometrical relations in dislocated crystals. *Acta Metall.* **1**, 153–162 (1953).
45. Shinjo, K. & Hirano, M. Dynamics of friction: superlubric state. *Surf. Sci.* **293**, 473–478 (1993).
46. Sangid, M. D., Ezaz, T., Sehitoglu, H. & Robertson, I. M. Energy of slip transmission and nucleation at grain boundaries. *Acta Mater.* **59**, 283–296 (2011).

Methods

Fabrication of graphene/hBN heterostructures. To transfer FLG over hBN steps, we used established aligned transfer techniques[47,48]. First, we exfoliated graphite and hBN flakes separately onto a SiO_2 (285 nm)/Si substrate with the scotch tape method. Then, a few-layer graphene flake was transferred onto a PDMS block by attaching the graphene/SiO_2/Si substrate onto PDMS and detaching the SiO_2/Si substrate using a KOH solution. The PDMS block was fixed to a micromanipulator and, finally, the FLG was transferred onto an exfoliated hBN flake containing terraces or steps. After the final transfer, we annealed the sample under high vacuum at 350 °C for 14 h.

TEM sample preparation. First, we evaporated a protective layer of amorphous carbon (5–30 nm thick) on top of the heterostructure. We then fabricated cross-sectional TEM samples using standard focused ion beam lift-out procedures in an FEI Helios 600i Dual Beam FIB-SEM system. Final milling was performed at 2 kV to reduce sample damage, using a cryo-can to minimize redeposition.

Aberration-corrected STEM imaging. The samples were imaged in a Thermo Fisher Scientific Themis Z aberration-corrected STEM. The STEM was operated at 80 kV, below the knock-on damage thresholds of graphene and hBN. We used a convergence angle of 25.2 mrad.

DFT calculations. Atomistic simulations of FLG bending were conducted using DFT[42,43], implemented by VASP[49] with projector augmented wave pseudopotentials[50]. A vdW-DF functional[51] was used to incorporate the van der Waals interaction between individual graphene layers. An energy cutoff of 400 eV was chosen for the plane wave basis, with a total energy convergence of 10^{-4} eV. An 80-atom graphene sheet was used for each layer, with a GGA-PBE lattice constant of 2.46 Å. The dimensions of the flat graphene were $2 \times 6 \times 1$, and 30 Å of vacuum was included to avoid interaction between adjacent images in the z direction in each supercell. A $2 \times 6 \times 1$ mesh was used to sample k-space points. To produce the deflection of graphene sheets, we reduced the size of the supercell in a given direction along the basal plane and we induced a geometric perturbation to produce out-of-plane deformation rather than in-plane strain. Through geometric optimization, we found the ground-state geometry of FLG for each supercell. Geometric relaxation was allowed until the forces on each atom were below 0.05 eV Å^{-1}. We used the fitting function $f(x) = \sum_{n=1}^{m} a_n \cos(b_n x)$ to describe the geometry of the deformed FLG, which enabled the evaluation of its curvature using $\kappa = \frac{|f''(x)|}{(1+f'(x)^2)^{\frac{3}{2}}}$. We found the bending energy of compressed multilayer graphene by subtracting the total energy of a flat, unstrained reference configuration from the total energy of the bent configuration with the same number of layers.

Classical potential simulations. Atomistic simulations of FLG are conducted using the Reactive Empirical Bond Order (REBO)[52] and Kolmogorov–Crespi (KC)[53,54] interatomic potentials, as implemented in the Large-scale Atomic/ Molecular Massively Parallel Simulator (LAMMPS)[55] package. We performed structural relaxation according to the damped dynamics minimization scheme 'fire'[56]. To ensure conformal bending of up to ten layers, each graphene sheet contains 50 unit cells in the zigzag direction and one in the armchair direction for a total of 200 carbon atoms. We analysed the structure (as detailed in the DFT section) to find the average curvature of compressed FLG and used the curvature and bending energy to find the average bending stiffness.

Data availability

The data and findings of this study are available from the corresponding authors on reasonable request.

References

47. Son, J. et al. Atomically precise graphene etch stops for three dimensional integrated systems from two dimensional material heterostructures. *Nat. Commun.* **9**, 3988 (2018).
48. Pizzocchero, F. et al. The hot pick-up technique for batch assembly of van der Waals heterostructures. *Nat. Commun.* **7**, 11894 (2016).
49. Kresse, G. & Furthmüller, J. Efficiency of ab-initio total energy calculations for metals and semiconductors using a plane-wave basis set. *Comput. Mater. Sci.* **6**, 15–50 (1996).
50. Blöchl, P. E. Projector augmented-wave method. *Phys. Rev. B* **50**, 17953–17979 (1994).
51. Klimeš, J., Bowler, D. R. & Michaelides, A. Van der Waals density functionals applied to solids. *Phys. Rev. B* **83**, 195131 (2011).
52. Brenner, D. W. et al. A second-generation reactive empirical bond order (REBO) potential energy expression for hydrocarbons. *J. Phys. Condens. Matter* **14**, 783–802 (2002).
53. Kolmogorov, A. N. & Crespi, V. H. Registry-dependent interlayer potential for graphitic systems. *Phys. Rev. B* **71**, 235415 (2005).
54. Ouyang, W., Mandelli, D., Urbakh, M. & Hod, O. Nanoserpents: graphene nanoribbon motion on two-dimensional hexagonal materials. *Nano Lett.* **18**, 6009–6016 (2018).
55. Plimpton, S. Fast parallel algorithms for short-range molecular dynamics. *J. Comput. Phys.* **117**, 1–19 (1995).
56. Bitzek, E., Koskinen, P., Gähler, F., Moseler, M. & Gumbsch, P. Structural relaxation made simple. *Phys. Rev. Lett.* **97**, 170201 (2006).

Author contributions

Under supervision by P.Y.H., E.H. performed TEM sample preparation, electron microscopy imaging and data analysis. Under supervision by P.Y.H. and A.M.v.d.Z., E.H. and J.Y. developed mechanics modelling and analysis. Under supervision by J.S. and A.M.v.d.Z., J.Y. and D.A.K. performed sample preparation and 2D heterostructure fabrication. Under supervision by E.E., J.Y. performed DFT calculations. Under supervision by E.E., E.A. performed simulations using classical force fields. K.W. and T.T. prepared high-quality hBN. All authors read and contributed to the manuscript.

Competing interests

The authors declare no competing interests.

Additional information

Supplementary information is available for this paper at https://doi.org/10.1038/s41563-019-0529-7.

Correspondence and requests for materials should be addressed to P.Y.H. or A.M.v.d.Z.

Reprints and permissions information is available at www.nature.com/reprints.